

Time-Resolved SAXS Study of Polarity- and Surfactant-Controlled Superlattice Transformations of Oleate-Capped Nanocubes During Solvent Removal

Zhong-Peng Lv,* Martin Kapuscinski, Gábor Járvas, Shun Yu, and Lennart Bergström*

Structural transformations and lattice expansion of oleate-capped iron oxide nanocube superlattices are studied by time-resolved small-angle X-ray scattering (SAXS) during solvent removal. The combination of conductor-like screening model for real solvents (COSMO-RS) theory with computational fluid dynamics (CFD) modeling provides information on the solvent composition and polarity during droplet evaporation. Evaporation-driven poor-solvent enrichment in the presence of free oleic acid results in the formation of superlattices with a tilted face-centered cubic (*fcc*) structure when the polarity reaches its maximum. The tilted *fcc* lattice expands subsequently during the removal of the poor solvent and eventually transforms to a regular simple cubic (*sc*) lattice during the final evaporation stage when only free oleic acid remains. Comparative studies show that both the increase in polarity as the poor solvent is enriched and the presence of a sufficient amount of added oleic acid is required to promote the formation of structurally diverse superlattices with large domain sizes.

removal)^[18,19] conditions, studies that probe how continuous changes in solvent composition influence the phase behavior are sparse.


Time-resolved small-angle X-ray scattering (SAXS) can yield information of the structural evolution of superlattices during removal and uptake of solvent^[11,20–23] and also of the lattice structure at both atomic levels when combined with wide-angle X-ray scattering (WAXS).^[24–26] Exposure of superlattices of oleic acid (OA) coated, cuboctahedral PbS and PbSe NPs to a nonpolar solvent (e.g., octane) was found to induce structural transformation between face-centered cubic (*fcc*), body-centered-tetragonal (*bct*), body-centered cubic (*bcc*) or hexagonal closed-packed (*hcp*) structures.^[11,24,27,28] Uptake of toluene was found to increase the interparticle distance and periodicity in superlattices of tetraoctylammonium bromide coated Au NP while exposure to ethanol resulted in an amorphous transformation.^[20] However, while SAXS and WAXS can yield structural information of the superlattice, the observed superlattice structures and phase transitions have to the best of our knowledge not been related to quantitative information of the solvent amount and composition.

In this study, time-resolved SAXS was used to study the structural transformation and lattice expansions during solvent removal of OA-coated iron oxide nanocube superlattices dispersed in a mixture of good and poor solvent with and without added OA. Multiphysics simulations of the evaporation of the

1. Introduction

Cubic nanoparticles can be assembled into superlattices and mesocrystals, in which the NPs display orientational and translational crystallographic coherence,^[1] with rich structural diversity and useful properties for a wide range of applications.^[2–5] The assembly of the superlattices is controlled by the size and shape of the NPs,^[6–8] the ligand- and solvent-mediated particle interactions,^[9–12] and the dynamics of the assembly and phase transition process.^[13–15] Although much insight has been obtained on the structural diversity of assemblies of cubic nanoparticles at static (dry)^[16,17] and dynamic (during solvent

Z.-P. Lv, M. Kapuscinski, L. Bergström
Department of Materials and Environmental Chemistry
Stockholm University
Stockholm SE-10691, Sweden
E-mail: lennart.bergstrom@mmk.su.se

 The ORCID identification number(s) for the author(s) of this article can be found under <https://doi.org/10.1002/smll.202106768>.

© 2022 The Authors. Small published by Wiley-VCH GmbH. This is an open access article under the terms of the Creative Commons Attribution License, which permits use, distribution and reproduction in any medium, provided the original work is properly cited.

DOI: 10.1002/smll.202106768

Z.-P. Lv
Department of Applied Physics
Aalto University
Espoo FI-00076, Finland
E-mail: zhongpeng.lyu@aalto.fi

M. Kapuscinski
Department of Materials Science and Engineering
Uppsala University
Uppsala SE-75103, Sweden

G. Járvas
Research Institute of Biomolecular and Chemical Engineering
University of Pannonia
Veszprem HU-8200, Hungary

S. Yu
Department of Materials and Surface Design
RISE Research Institute of Sweden
Lund SE-22370, Sweden

mixed solvents from the levitating drops were used to correlate how the nanoparticle concentration, solvent composition, and polarity, influenced the structural transformations, domain size, and lattice expansion during solvent removal. Additional insight on the structural transformations was provided by simulations of SAXS patterns of superlattices with cubic building blocks with different orientations. This study elucidates that the composition and polarity of the solvent during the final solvent removal step can control the complex structural transformations and interparticle separation distance within oleate-capped nanoparticle superlattices.

2. Results and Discussion

Time-resolved SAXS measurements on oleate-capped iron oxide truncated nanocubes (TCs) dispersed in evaporating levitating droplets were performed using the experimental setup shown in **Figure 1a**. The oleate-capped iron oxide TCs with a concentration c_{TC} were dispersed in a good solvent (GS)/poor solvent (PS) mixture of octane and 1-pentanol of different volume ratios (V_{GS}/V_{PS}) and added OA (V_{OA})^[29] (**Table 1**). The evaporation rate of the solvents and the time-dependent solvent composition were estimated by a combination of density

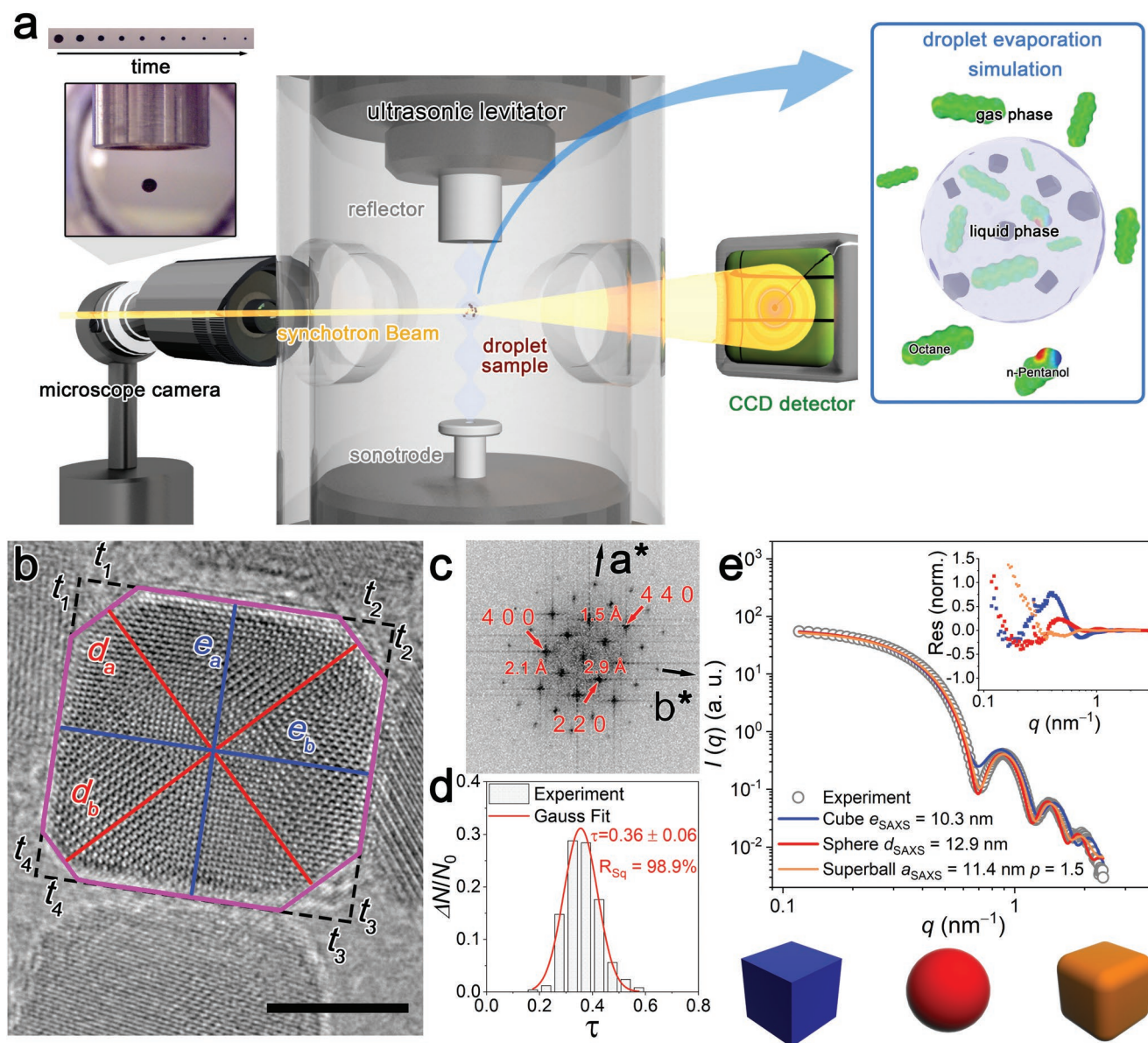


Figure 1. Experimental set-up and characteristics of the investigated nanocubes: a) Schematic illustration of how the structural evolution, particle concentration, and solvent composition of TC dispersions in an evaporating levitating droplet is monitored by a combination of real-time SAXS, microscope camera, and simulation of the evaporation. b) HRTEM image of a TC particle and its geometric parameters. c) FFT pattern of a diluted dispersion of TCs (hollow grey spheres) with fits using a cubic (blue), a spherical (red) and a superball (orange) form factor. The normalized residuals of the three fittings are indicated in the inset. The illustrations below correspond to a 10.3 nm edge length cube (blue), a 12.9 nm diameter sphere (red), and a 11.4 nm edge length superball with $p = 1.5$ (orange), respectively.

Table 1. Composition of TCs dispersed in a mixture of good solvent (GS) and poor solvent (PS) with added oleic acid (OA).

Sample ID	$V_{GS}:V_{PS}^a)$	c_{TC} [mg mL ⁻¹]	V_{OA} [μL mL ⁻¹]	$[OA]_{free}^b)$ [mM]
GP48	5:1	3	4.8	15.2
GP0	5:1	3	0	0
G48	1:0	3	4.8	15.2
GP6	5:1	3	0.6	1.9

^{a)}GS and PS were for all samples octane and 1-pentanol; ^{b)} $[OA]_{free}$ is calculated by $[OA]_{free} = \frac{V_{OA} \times \rho_{OA}}{M_{OA}}$.

functional theory (DFT) and statistical thermodynamics at the molecular scale (COSMO-RS theory), with a mass-transport computational fluid dynamics (CFD) model (see Methods for details).

Transmission electron microscopy (TEM) analysis shows that the TCs (Figure 1b) have a narrow Gaussian-shaped edge-length distribution with a mean edge length of $e_{TEM} = 10.8$ nm and a size dispersity (SD) of 0.06, defined as the quotient of standard deviation and mean edge length (Figure S1, Supporting Information). The d -spacing obtained from the fast Fourier transform (FFT) pattern in Figure 1c fits the d -spacing of magnetite and/or maghemite very well where 2.96 Å for (220), 2.09 Å for (400), and 1.48 Å for (440). Figure 1d shows that the TCs have a mean degree of truncation, $\tau = 0.37 \pm 0.06$ (0 for ideal cube and 1 for cuboctahedron), determined from the lengths of the two diagonals (d_a and d_b) and the edge lengths (e_a and e_b).

Statistic size and shape information has also been obtained by fitting the form factor $P(q)$ for cubic, spherical, and superball morphologies to the SAXS data of a dilute TC dispersion, where $I(q) = P(q)$. Using a fixed SD = 0.06, we obtain an edge length of $e_{SAXS} = 10.3$ nm using a cubic form factor, a diameter of $d_{SAXS} = 12.9$ nm using a spherical form factor, and an edge length of $a_{SAXS} = 11.4$ nm with $p = 1.5$, which corresponds to $\tau = 0.41$, using a superball form factor (Figure 1e).^[30] The normalized residuals of the fitting results (see inset Figure 1e) show that the superball mode fits with our experimental curve better than the spherical and cubic modes in the high q region ($q > 0.3$ nm⁻¹), which is consistent with the truncated cube morphology of the TCs. Indeed, the normalized residuals also suggest that the spherical model fits the data better than the cubic model.^[22] Because there is no superball mode available for structure factor and lattice parameter fitting, we chose to use a spherical form factor for the subsequent analysis of the SAXS data.

Figure 2a,b shows the time-dependent SAXS and shrinkage data of the evaporating droplet of GP48, which is a 3 mg mL⁻¹ TC dispersion in a 5:1 (v:v) mixture of good-solvent octane and poor-solvent 1-pentanol, to which 4.8 μL mL⁻¹ OA had been added. The shrinkage data and the simulations of the compositional changes of the evaporating solvent mixture (Figure 2c) show that the evaporation of the mixed-solvent droplet proceeds in two major stages: a fast evaporation stage where the good-solvent octane with low-boiling point/high partial pressure evaporated ($t = 0$ s to 190 s) rapidly, and a slow evaporation stage where the remaining poor-solvent 1-pentanol with high-boiling point/low partial pressure evaporated ($t = 190$ s to 650 s) slowly.

The simulated compositional changes (Figure 2c) were used to estimate the time-dependent polarity; Figure 2d shows that the dielectric constant ϵ increased from 4 to close to 14 during the first evaporation stage, then decreased slowly from 13 to about 10 between $t = 200$ s to 500 s, and finally decreased rapidly to $\epsilon = 3.1$ at the end of the second (slow) evaporation stage ($t = 650$ s).

The fcc structural peak in the SAXS pattern in Figure 2a, which indicates the formation of ordered superlattices by nanocube assembly, first appeared at $t = 154$ s when the polarity was $\epsilon = 12.3$ and ended at $t = 219$ s when ϵ reached its maximum value of 13.7. The fcc lattice has a unit cell dimension a of 22.0 nm with an average characteristic length and an average displacement from the ideal lattice point (Debye–Waller factor) of 151 nm and 2.51 nm, respectively (Table 2 and Figure S2a, Supporting Information). It should be noted that the unit cell dimension, characteristic length, and displacement of the superlattices were analyzed using a spherical form factor with $d = 12.9$ nm and SD = 0.06 with the program Scatter^[31] and we have not made a detailed analysis taking into account, e.g., the beam shape and detector pixel size. Hence, the obtained values for the characteristic length have mainly been used to follow changes during the solvent removal process.

We have evaluated how the SAXS patterns are affected by the orientation of the particles by simulating the scattering patterns of tilted fcc (super)lattices of 10.8 nm cubes that were extrinsically rotated 11.25° stepwise from 0° to 90° on each axis, resulting in simulated SAXS patterns for 729 different orientations. The nanocube orientation has a significant influence on the relative intensity of the different peaks in the simulated SAXS patterns due to the anisotropic electron density distribution of the cubic building block, which is not present in a superlattice of spherical particles.^[32–34] The simulations show that the (200)_{super} peak at $q = 0.57$ nm⁻¹ and (220)_{super} peak at $q = 0.80$ nm⁻¹ is more pronounced while the (400)_{super} peak at $q = 1.14$ nm⁻¹ and the (331)_{super} peak at $q = 1.24$ nm⁻¹ are weaker in lattices with high tilting angles (close to 45°), than in the less-tilted lattices (Figure S3a, Supporting Information). Comparison of the experimental and calculated (200)_{super}, (220)_{super}, and (400)_{super} peaks shows that the SAXS pattern of tilted fcc lattice with orientation on x -, y -, z -axis of (35.26°, 30°, 54.74°) fits the experimental pattern for the initially formed superlattice much better than the non-tilted fcc lattice (Figure 3a,b). The tilted fcc lattice is consistent with the TCs being packed face-to-face along the [111]_{super} direction, with a unit cell parameter $a = (3e_{TC} + 6l_{OA})/\sqrt{3}$, which corresponds to an estimated l_{OA} of 1 nm. Hence, the structural analysis suggests that the OA capping agent is compressed or folded, which has been shown to occur in high-polarity solvents.^[35]

During the second stage of solvent removal, from 219 s to 650 s, the SAXS patterns did not indicate any structural transformations (Figure 2a). The SAXS patterns displayed several changes during the final solvent removal stage, $t > 650$ s, when the high-boiling point solvent 1-pentanol has evaporated and the nanocubes and superlattices are dispersed in mainly free oleic acid (Figure 2a). Specifically, the decreasing intensity of the (111)_{super} peak of fcc from $t = 700$ s to 800 s and the appearance of a broad peak at $q = 0.35$ to 0.40 nm⁻¹ in the SAXS pattern (the yellow dash line box in Figure 2a) suggests

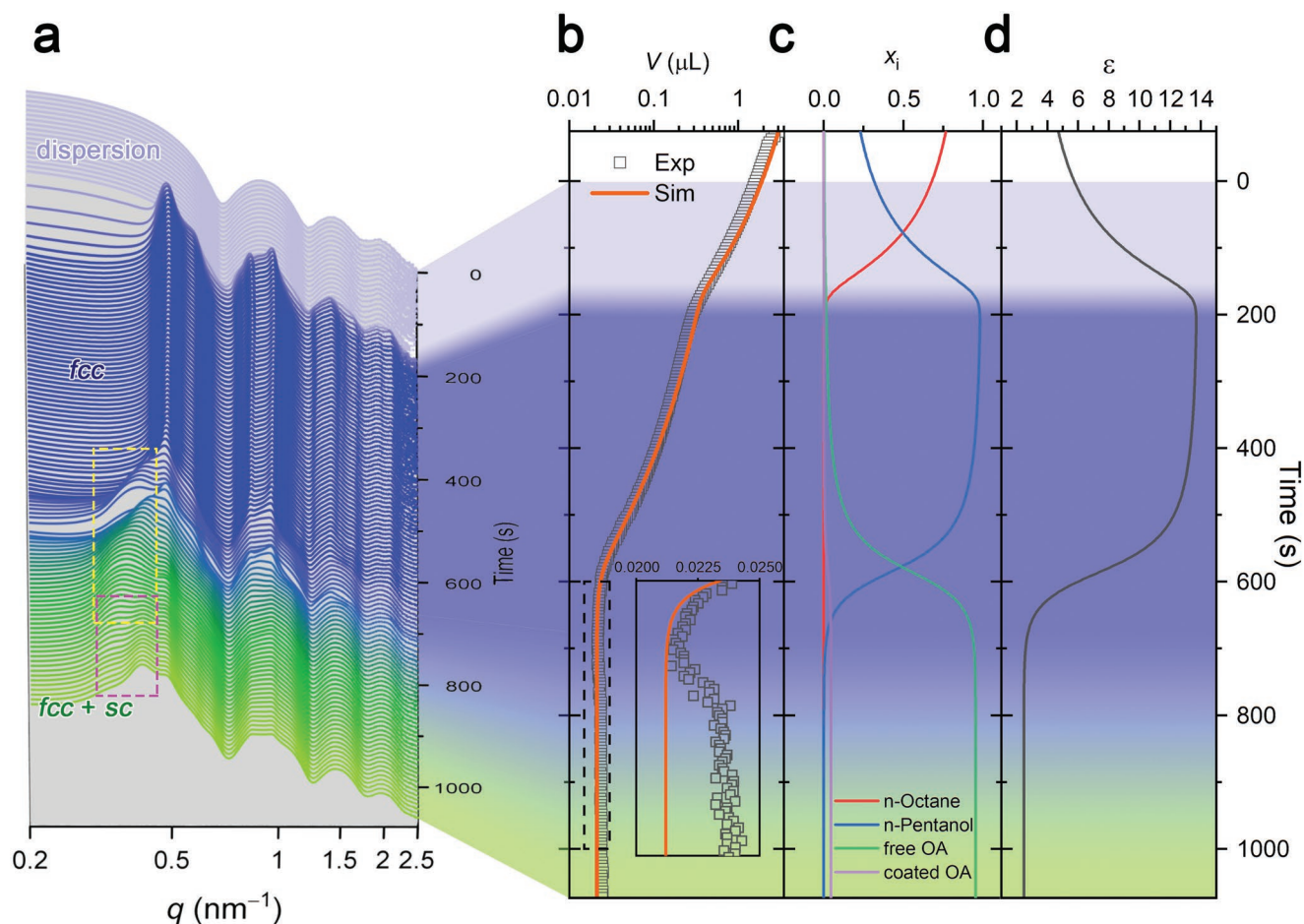


Figure 2. Time-dependent SAXS data and composition of TC dispersions in an evaporating droplet of dispersion with added oleic acid (GP48). a) Time-dependent 1D SAXS curves of an evaporating droplet of TCs dispersed in a good solvent: poor solvent mixture with added oleic acid (OA) (GP48). Patterns of dispersion, *fcc*, and *fcc + sc* stages of TCs were indicated by light blue, dark blue, and green, respectively. The yellow and purple dash line boxes indicate the appearance and disappearance of a structural peak at $q = 0.35 - 0.40 \text{ nm}^{-1}$ during the transformation. b) Experimental (hollow cubic dots) and simulated (orange curve) time-dependent droplet volume. The inset displays the region from $t = 600 \text{ s}$ to 1000 s marked by the dashed rectangle. c) Time-dependent mole fraction (x_i) of the organic species in the droplet obtained from simulations. d) Time-dependent dielectric constant (ϵ) of the solvent mixture in the droplet, where $\epsilon = \sum \epsilon_i \times x_i$.

Table 2. Structural characteristics of superlattices formed by TC assembly in a shrinking evaporating droplet. The SAXS data was fitted using a spherical form factor with 12.9 nm diameter and SD = 0.06, obtained from analysis of dilute dispersions, Figure S2 (Supporting Information).

Sample ID	Time [s]	Lattice type	a [nm]	characteristic length [nm]	Displacement [nm]	Packing Density (φ) ^{a)}
GP48	219	<i>fcc</i>	22.0	151	2.51	0.47
	1075	<i>sc</i>	15.2	95	3.31	0.35
	1075	<i>fcc</i>	22.8	95	3.31	0.43
GP0	245	<i>fcc</i>	21.5	113	2.65	0.51
	1368	<i>fcc</i>	22.8	91	3.33	0.43
G48	368	<i>fcc</i>	22.9	65	2.37	0.42
	1086	<i>fcc</i>	26.6	60	3.09	0.27
GP6	254	<i>fcc</i>	21.7	123	2.07	0.49
	1308	<i>fcc</i>	22.3	113	2.58	0.45

^{a)}The packing density represents the volume fraction of TC core in the unit cell given as, $\varphi = 4e_{TC}^3/a^3$ for *fcc* lattice, and e_{TC}^3/a^3 for *sc* lattice.

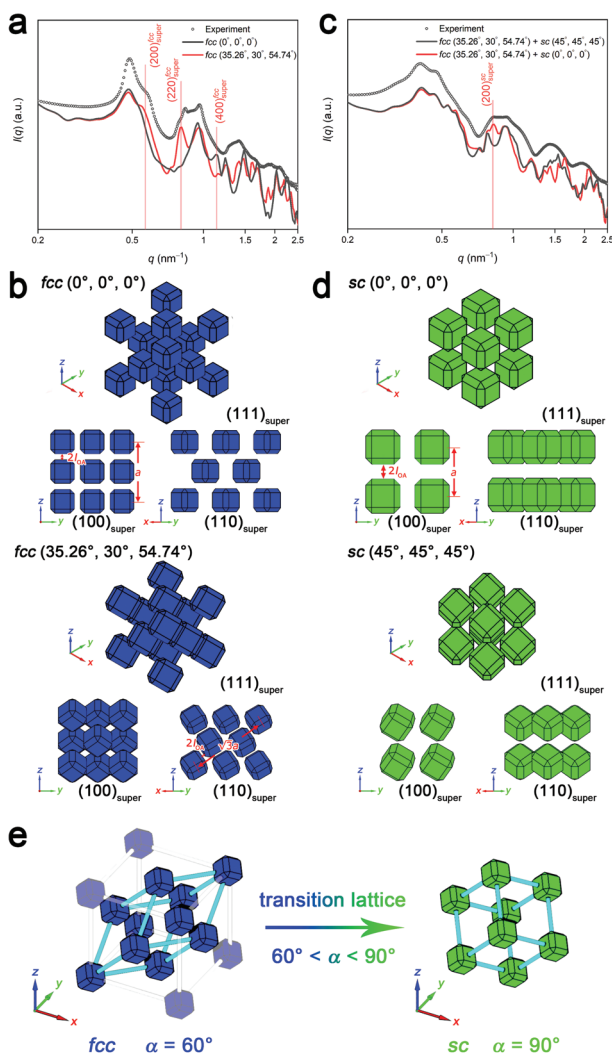


Figure 3. Structural transformations of TC superlattices in GP48. a) Calculated SAXS curves of nanocubes arranged in a regular (non-tilted) *fcc* lattice (black curve) and tilted *fcc* lattice (red curve), and experimental SAXS pattern at $t = 219$ s (black dot curve) of the GP48 system. Selected reflections are indicated as red vertical lines. b) Illustration of the arrangement in different directions of nanocubes packed in a non-tilted *fcc* lattice (top) and tilted *fcc* lattice (bottom). The orientations of the TCs are $(0^\circ, 0^\circ, 0^\circ)$ and $(35.26^\circ, 30^\circ, 54.74^\circ)$ respectively. c) Calculated SAXS curves of mixtures of tilted *fcc* lattice and regular simple cubic (*sc*) lattice (red curve); and tilted *fcc* lattice and tilted *sc* (black curve), and the experimental SAXS pattern obtained at $t = 1075$ s (black dot curve) of the GP48 system. Selected reflections are indicated as red vertical lines. d) Illustration of the arrangement in different directions of nanocubes packed in a nontilted *sc* lattice (top) and tilted *sc* lattice (bottom). The orientations of the TCs are $(0^\circ, 0^\circ, 0^\circ)$ and $(45^\circ, 45^\circ, 45^\circ)$ respectively. e) A schematic illustration of the structural transformation from tilted-*fcc* to a regular (non-tilted) *sc* lattice.

a structural transformation of the superlattice. This broad peak that represents the transition lattice, gradually disappears and another peak at $\approx q = 0.41 \text{ nm}^{-1}$ appears at $t = 800$ s to 1075 s, which implies that the structural transformation proceeded well into the final evaporation stage (the purple dashed line box in Figure 2a). Fitting the SAXS pattern at $t = 1075$ s with a

spherical particle model, indicates that there are two different lattices present in the assembly; the original *fcc* lattice with $a = 22.8$ nm and a new *sc* lattice with $a = 15.2$ nm (Figure S2b, Supporting Information).

Comparison of the simulated and experimental peak intensity of the $(111)_{\text{super}}$, $(200)_{\text{super}}$, and $(211)_{\text{super}}$ peaks of the *sc* lattice (Figure S3b, Supporting Information) showed that the *sc* lattice is probably non-tilted $(0^\circ, 0^\circ, 0^\circ)$. This orientation is also reasonable from an energetic point of view as face-to-face packing has the lowest energy. The comparison of the $(200)_{\text{super}}$ peak of the simulated SAXS curves for different structures and orientations with the experimental data in Figure 3c,d, confirms that the SAXS curve of a non-tilted *sc* lattice fits well with the experimental data. The non-tilted *sc* lattice have a lattice constant $a = 15.2$ nm, which corresponds to a length of the OA capping agent; $l_{\text{OA}} = (a - e_{\text{TC}})/2 = 2.2$ nm.^[36] This analysis suggests that the OA attains a fully stretched conformation in the non-tilted *sc* lattice that forms at the end of the solvent removal when the polarity of the remaining medium has become very low ($\epsilon = 2.4$) (Figure 2d).

It is interesting to note that the structural transformation is associated with an increase in the volume of the droplet of about 10% (Figure 2b). The expansion is related to the increase of the length of the OA capping agent from about 1 to 2.2 nm as the superlattice transforms from a tilted *fcc* lattice to a non-tilted *sc* lattice (Figure 3e) and a decrease of the packing density (ϕ) from 0.47 of the tilted *fcc* to 0.35 of the non-tilted *sc* lattice (Table 2, and Method S1, Supporting Information). The crystal angle α in the primitive cell of *fcc* unit cell increases from 60° to 90° during the transformation but the TCs did not rotate during the structural transformation. It is interesting to note that while *sc* to *fcc* or *fcc* to *bcc* structural transformations during evaporation-driven superlattice assembly have been observed before,^[14,18] this is to the best of our knowledge the first report of an *fcc* to *sc* transformation. The structural transformation during the final solvent removal step is also associated with a decrease of the estimated characteristic length from 161 nm to 95 nm and a moderately increased displacement from 2.51 nm to 3.31 nm (Table 2), which indicates that domains with smaller size and a higher degree of defects were formed during the transition.

In a comparative system, we have followed the assembly and structural transformations during solvent removal of a TC dispersion in a 5:1 GS:PS mixture without any added OA, GP0 (Table 1). Time-resolved SAXS data could be retrieved (Figure 4a) although the shrinkage of the GP0 droplet was disturbed by the growth and bursting of a bubble within the drying droplet during the second solvent removal stage that was initiated at $t = 500$ s (Figure 4b and Figure S4, Supporting Information). Analysis of the SAXS data during the first evaporation stage (data sampled at $t = 245$ s, Figure S2c, Supporting Information) showed that the *fcc* lattice of GP0 has a smaller a (21.5 nm) and characteristic length (113 nm) than GP48 (22.0 nm and 151 nm, respectively) and a similar displacement of 2.65 nm (Table 2). This suggests that free OA in the dispersions with added OA (GP48) increased the inter-particle spacing and promoted the growth of large superlattices, which corresponds well to previous studies that concluded that the addition of free OA is required to form large and well-ordered

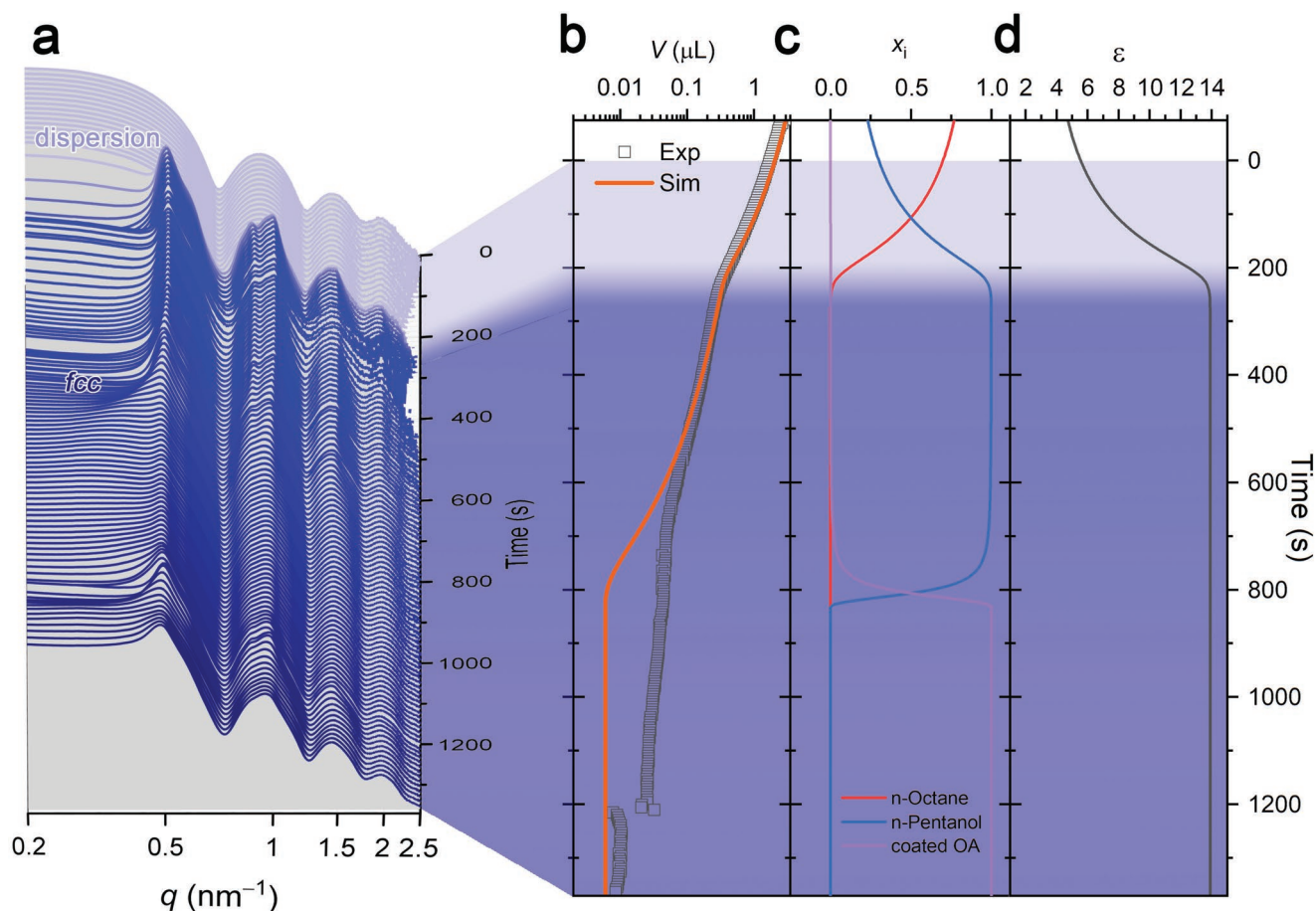


Figure 4. Time-dependent SAXS data and composition of TC dispersions in an evaporating droplet without added oleic acid (GP0). a) Time-dependent 1D SAXS curves of an evaporating droplet of TCs dispersed in good solvent: poor solvent mixture without any added oleic acid (OA) (GP0). Patterns of dispersion and *fcc* stages of TCs were indicated by light blue, and dark blue, respectively. b) Experimental (hollow cubic dots) and simulated (orange curve) time-dependent droplet volume of GP0. c) Time-dependent mole fraction (x_i) of the organic species in the droplet obtained from simulations. d) Time-dependent dielectric constant (ϵ) of the solvent mixture in the droplet, where $\epsilon = \sum \epsilon_i \times x_i$.

superlattices from oleate-capped nanoparticles by evaporation-driven self-assembly.^[29,37]

No structural transformation could be deduced from the SAXS data during $t = 245$ to 600 s of the second stage of solvent removal when the medium is dominated by 1-pentanol (Figure 4c) and the polarity remained unchanged at $\epsilon = 13.7$ (Figure 4d). Although no lattice transformation occurred during the lattice expansion, the displacement increased dramatically from 2.65 nm to 3.33 nm and the characteristic length slightly decreased from 113 nm to 91 nm (Figure S2d, Supporting Information). The lattice has remained essentially unaffected at $t > 800$ s, when only a little solvent remained in the droplet.

Time-resolved SAXS data of superlattices assembled from a TC dispersion with an initial GS:PS ratio of 5:1 and only 0.6 $\mu\text{L mL}^{-1}$ of added OA (GP6) did not display any visible structural transformation during solvent removal (Figure S5, Supporting Information). We hypothesize that a sufficient amount of free OA is required to enable a transformation from a tilted *fcc* lattice to a non-tilted *sc* lattice, as, e.g., observed for the GP48 system with 4.8 $\mu\text{L mL}^{-1}$ of added OA (Figure 2a). Table 2 shows that the as-assembled *fcc* lattice of GP6 was characterized by a larger characteristic length (123 nm) and smaller displacement

(2.07 nm) than GP0. However, the superlattices became more disordered after the final solvent removal ($t > 800$ s), similar to GP0. This indicates that even a small amount of added OA is crucial to reduce the defect level in superlattices formed by an evaporation-driven poor-solvent destabilization process.

We have also investigated a dispersion that is dispersed in a good solvent (octane) and 4.8 $\mu\text{L mL}^{-1}$ of added OA, G48 (Table 1). The first indication of the formation of superlattices in the time-resolved SAXS data (Figure 5a) occurred at around $t = 317$ s when the TC concentration is about 360 mg mL^{-1} (Figure 5b), which is significantly higher than the critical particle concentration for crystallization of about 20 mg mL^{-1} that was found in the poor-solvent containing dispersions GP48, GP0, and GP6. The superlattices that formed in the G48 system have a small characteristic length of 65 nm and a displacement of 2.37 nm, obtained from SAXS curve fitting (Table 2 and Figure S2g, Supporting Information). During the final solvent removal stage from $t = 700$ s to 780 s, the lattice dramatically expanded from $a = 22.9$ nm to 26.6 nm, and $d_{(111)\text{super}}$ increased by 1.5 nm, from 14.0 nm to 15.5 nm. The displacement also increased to 3.09 nm, suggesting that the superlattices became more disordered. The polarity change of G48 is

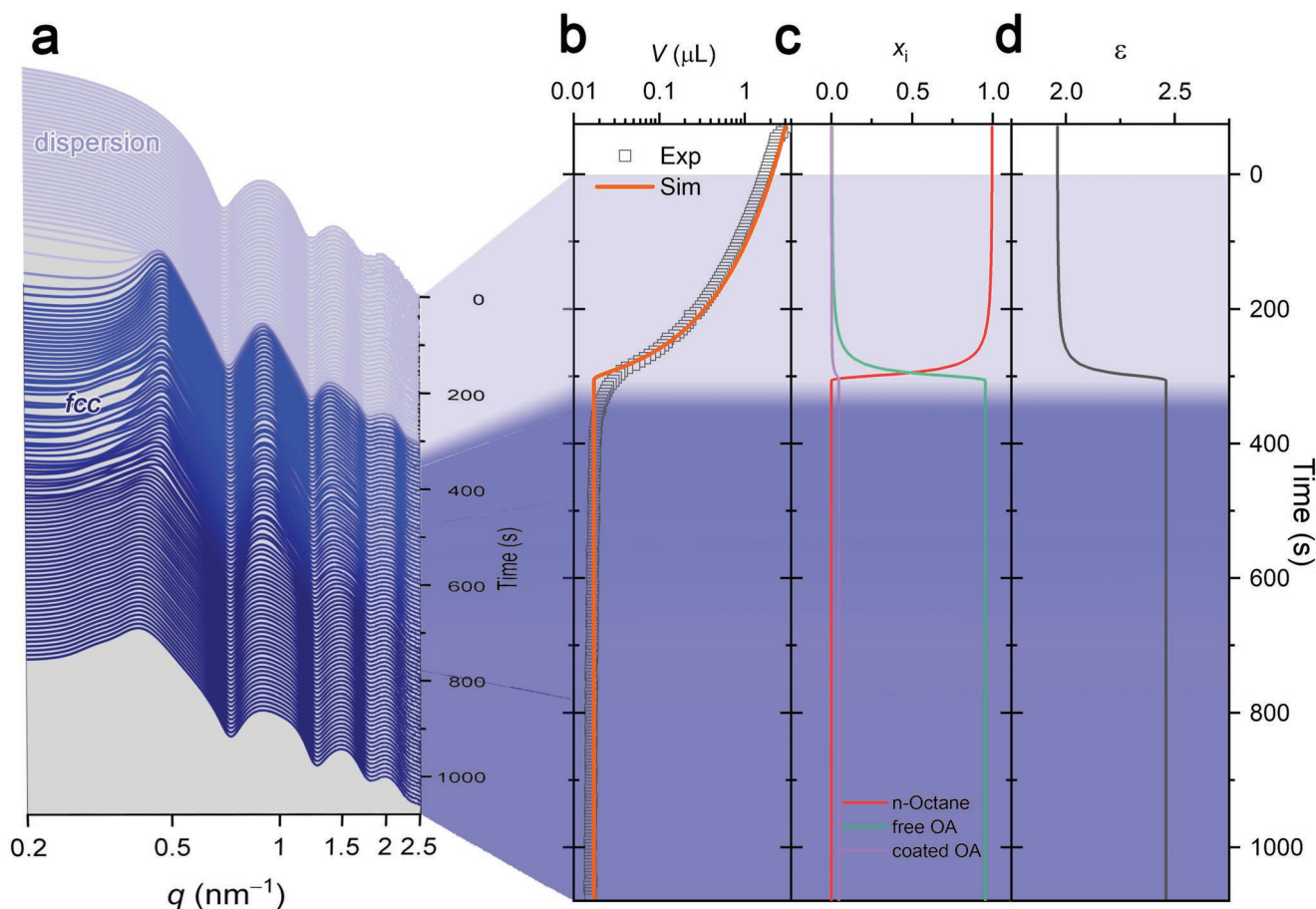


Figure 5. Time-dependent SAXS data and composition of TC dispersed in only octane with added oleic acid (G48). a) Time-dependent 1D SAXS curves of an evaporating droplet of TCs dispersed in only good solvent with added oleic acid (G48). Patterns of dispersion and *fcc* stages of TCs were indicated by light blue, and dark blue, respectively. b) Experimental (hollow cubic dots) and simulated (orange curve) time-dependent droplet volume of G48. c) Time-dependent mole fraction (x_i) of the organic species in the droplet obtained from simulations. d) Time-dependent dielectric constant (ϵ) of the solvent mixture in the droplet, where $\epsilon = \sum \epsilon_i \times x_i$.

small, $\epsilon = 1.96$ and 2.46 before and after the assembly stage, respectively (Figure 5d), compared to the comparative poor-solvent containing system (GP48), where the dielectric constant first increased and then decreased. It is worth noting that the droplet volume decreased constantly during the evaporation in G48, meaning that the lattice expansion is caused by free OA intercalation rather than the stretching of coating OA in GP48, which was induced by polarity changing.

Figure 6a illustrates the folded structure of the alkyl chains of the attached (grafted) OA in high polarity solvents and that the alkyl chains extension into the solvent increased as the solvent polarity is reduced.^[35] The free OA concentration ($[OA]_{\text{free}}$ in Table 1) can both increase the surface ligand coverage of the particles and also act as a solvent that inhibits structural arrest. The three dispersions GP48, GP6, and GP0 contain equal ratios of good solvent and poor solvent but exhibit significant differences during the final drying stage, which is due to their different free OA concentrations. Figure 6b shows the estimated surface coverage of OA that is based on adsorption isotherms presented in a previous study.^[38] The coverage of grafted OA for GP0 was estimated to be 2.0 OA nm^{-2} . The physisorption of OA increases with increasing $[OA]_{\text{free}}$, resulting in an

increasing OA surface coverage, which plays an important role in the superlattice formation.^[39] The observation of less defects in GP6 and GP48 and that the unusual *fcc* to *sc* transition only occurs in GP48 suggests that both a ligand saturated surface and a sufficient amount of unbound OA is needed to facilitate the phase transition.

3. Conclusion

Time-resolved in situ SAXS measurements of OA-capped TC superlattices in levitating droplets during solvent evaporation have been correlated to estimates of the solvent composition to shed light on the impact of the solvent polarity and free OA on the superlattice structure. Simulation methods were employed for a thorough analysis of both the solvent composition during solvent evaporation as well as the orientation of the TCs in the superlattices. We found that formation of superlattices with a tilted face-centered cubic (*fcc*) structure and folded OA capping molecules by assembly of the TCs by evaporation-driven poor-solvent enrichment in the presence of free oleic acid occurred when the polarity reached its maximum. The tilted *fcc* lattice

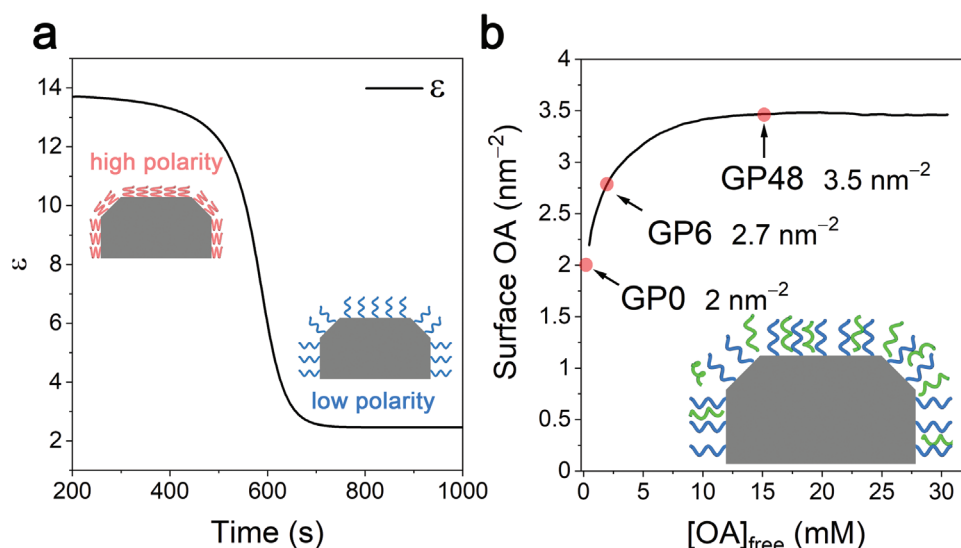


Figure 6. Mechanism of the *fcc* to *sc* transition in oleate-capped TCs dispersed in mixed solvents with free OA. a) The extension of the grafted OA increases with decreasing polarity. b) Estimated Surface OA coverage as a function of free OA concentration. The surface OA coverage for **GP48**, **GP6**, and **GP0** are indicated on the curves as red dots. The inserted illustration shows grafted (blue) and physisorbed (green) OA molecules on the TC surface.

expanded as the poor solvent evaporated and the superlattice eventually transformed to a regular simple cubic (*sc*) structure during the final evaporation stage when only free oleic acid remained. This unusual tilted *fcc* to regular *sc* lattice transformation was associated with a 10% volume increase of the droplet volume and an unfolding of the OA capping molecules. The intensity modulation at higher q was used to evaluate the orientation mismatch between nanocube and the superlattice, i.e., the tilt, during the phase transition. Comparative experiments showed that the presence of both the poor-solvent and sufficient OA in the mixture is essential for the transformation to occur. The understanding of how free OA and surface bound OA, as well as polarity control superlattice structures could be applied to metallic and inorganic nanoparticles coated by hydrophobic surfactants such as oleic acid or oleylamine, which paves a way for the assembly of anisotropic nanoparticles for, e.g., electronic and photonic applications.

4. Experimental Section

Synthesis and Purification of TCs: In a typical synthesis, ferric oleate (5 mmol),^[40] Oleic acid (0.7 mmol, 99%, TCI), sodium oleate (0.7 mmol, 97%, TCI), 1-octadecene (25 mL, 90%, Aldrich), and 1-hexadecene (5 mL, 92%, Aldrich) were mixed under a moderate inert gas flow. The mixture was first heated to 140 °C and kept for 30 min. Under a blanket of inert gas, the mixture was then heated to 315 °C at 3 °C min⁻¹ and kept at this temperature for 30 min. After rapidly cooling to room temperature, the mixture was thoroughly washed with ethanol and toluene. The dispersion was then vacuum dried at 60 °C and stored at 4 °C under inert gas to obtain approximately 900–1000 mg tar-like product, consisting of \approx 40%–50% iron oxide. The tar-like synthesis product was further purified by repeated re-dispersion and magnetic separation in a mixture of octane (98%, Sigma-Aldrich) and 1-pentanol (99%, Sigma-Aldrich). After four washing cycles, a purified black powder containing iron oxide TCs was separated using a magnet. Thermogravimetric analysis (Discovery TGA 1, TA Instrument, USA) of the purified TCs showed they contained 91 wt% of iron oxide and 9 wt% OA corresponding to an OA coverage

of 2.0 molecules nm^{-2} . Samples for the SAXS experiment were obtained by re-dispersing the purified TCs in different solvents as listed in Table 1. All chemicals were used without further purification and purchased from commercial sources.

Microscopic Characterization: TEM and high-resolution TEM (HRTEM) of individual TCs were performed on a JEOL JEM-2100F microscope (JEOL, Japan) operated at 200 kV, by drop-casting the purified TC dispersion in toluene onto a copper grid. Fast Fourier transform (FFT) of the HRSEM/HRTEM was performed by ImageJ (<https://imagej.nih.gov/ij/>). The particle sizes for statistics in Figure 1 and Figure S1 (Supporting Information) were measured by Nano Measurer (Department of Chemistry, Fudan University) from TEM images with a spatial resolution of 0.2 nm (corresponding to a 2% systematic error). To measure the shape anisotropy, the dimensionless degree of truncation can be defined as $\tau = \frac{t_1 + t_2 + t_3 + t_4}{e_a + e_b}$ ($\tau = 0$ is an ideal cube, $\tau = 1$ is a cuboctahedron), where t_1 – t_4 are the truncated lengths at vertices.^[22] τ of an individual TC was calculated from the lengths of its two diagonals (d_a and d_b) and the edge lengths (e_a and e_b) using:

$$\tau = \frac{2\sqrt{2} \times \sqrt{e_a^2 + e_b^2} - \sqrt{2} \times (d_a + d_b)}{e_a + e_b} \quad (1)$$

Real-Time SAXS Measurement: Scattering experiments were carried out at the P03 beamline at DESY, Hamburg, Germany.^[41–43] The data was recorded by a Pilatus 1M detector covering a range of $0.11 \text{ nm}^{-1} < q < 3.59 \text{ nm}^{-1}$. The time-resolved data was acquired with an exposure time of 0.5 s per frame resulting in a time resolution of 0.9 s. The 2D data was reduced and integrated to a 1D pattern using the program DPDAK.^[44] The colloidal droplet was injected into an acoustic levitator (model 13K11, tec5, Oberursel, Germany) and irradiated by a square-shaped beam with a spot size of $20 \times 20 \mu\text{m}^2$ and a wavelength $\lambda = 0.96 \text{ \AA}$. A frame of the raw 2D SAXS pattern was given in Figure S6, Supporting Information, which indicates an isotropic powder-like sample.

The droplet was simultaneously observed with a microscope camera to correlate the onset of crystallization to the concentration. The video was decomposed into image frames with the program VirtualDub. The radii a and c of the oblate ellipsoidal droplet were obtained by analyzing the image frames with ImageJ and the droplet volume was calculated by $V_{\text{DL}}(t) = \frac{4}{3}\pi a^2 c$. The time-dependent concentration can be calculated by

$c_{DL}(t) = \frac{c_{DL}(0)V_{DL}(0)}{V_{DL}(t)}$ with $c_{DL}(0)$ and $V_{DL}(0)$ as the initial concentration and volume, respectively.

Fitting the SAXS Curve: The experimental SAXS curve of a dilute TC dispersion was fitted with a spherical, cubic form factor, and superball form factor^[30] using the program SasView. The first frame of the time-resolved measurements, when the dispersions were free of aggregates and the contribution to the scattered intensity can be assumed to be purely by the form factor, was used for the fitting. For lattice parameter fitting, the 1D SAXS curves of the superlattices were fitted and calculated with the program Scatter^[31] using the built-in *fcc*, *sc*, *hcp*, and *bcc* lattice model with spherical particles having a core diameter of 12.9 nm and SD of 0.06. The comparison fitting using different lattice models can be found in Figure S2i,j, Supporting Information. For fitting the characteristic length, the (111)_{super} peak and (100)_{super} peak were used for *fcc* lattice and *sc* lattice, respectively.

Simulation of the Droplet Evaporation: The mixture of n-Octane, n-Pentanol, and oleic acid was a non-ideal solution, thus their single droplet evaporation was simulated by combining the COSMO-RS thermodynamics method with a mass transport model utilizing computational fluid dynamics as reported earlier.^[45] Shortly, the estimated liquid phase properties were used to calculate the vapor-liquid equilibrium of the ternary mixtures (please note, solid-phase nanoparticles were not considered for evaporation modeling), which were necessary for the subsequent gas-phase evaporation flux calculation. The rate of gas-phase transport was derived by utilizing the Maxwell–Stefan diffusion and convection theory. Evaporating droplets were subjected to cooling due to the enthalpy change of the evaporation process. A modified infinite conductivity approach was used to compute the heat balance of the evaporating droplets during the simulation procedures with 0.1 °C accuracies.^[45] The raw time-dependent volume data was corrected by applying a scale factor of 1.5 or 1.8 and a TC volume of 0.006 or 0.003 μL. This methodology resulted in high resolution, time-dependent physical-chemical properties, which were difficult to measure experimentally, such as the activity coefficients of the components, the liquid phase compositions, and the cumulative and components evaporation rates.

SAXS Profile Calculation: The theoretical calculation of SAXS line-profile in Figure 3 and Figure S3, Supporting Information is completed via python programming language in the coordination of a 3D reciprocal space. The theoretical intensity is defined as

$$I = \text{scale} \cdot \left| F(q_x, q_y, q_z, R) \right|^2 \cdot S(q_x, q_y, q_z, L) \quad (2)$$

where, q_x , q_y , and q_z , are wavevectors in reciprocal space, R and L are half the length of a nanocube edge and the lattice constant of the mesocrystal, respectively; and scale is a scaling factor. $F(q, R)$ is the form factor which takes the form of a nanocube as^[46]

$$F(q, R) = V_{\text{cube}} \cdot \text{sinc}(q_x R) \text{sinc}(q_y R) \text{sinc}(q_z R) \quad (3)$$

q_x , q_y , and q_z are decomposed wavevector, q , in cartesian coordination.^[46] $S(q_x, q_y, q_z, L)$ is the structure factor of an assembled crystal, for example, the reciprocal space of a simple cubic packing is also simple cubic and that of a face-center cubic packing has a body-centered symmetry. The structure factor is convoluted via a Lorentzian function to simulate the peak broadening.

Two identical 3D reciprocal spaces are created for form factor and structure factor, respectively, by defining the 3D data arrays with axes, representing (100)_{super}, (010)_{super}, and (001)_{super}, and labeled as x , y , and z . In this case, the nanocube orientation is aligned with the lattice axes. Each element in the 3D data arrays is a calculated scattering intensity of form factor or structure factor. The total intensity is calculated via the element-wise multiplication of the form factor and structure factor arrays. When the nanocube is rotated inside the lattice system, the structure factor remains in its initial orientation, whereas the form factor is subject to a rotation transformation, which is re-calculated first via

the Rotation operation of `scipy.spatial.transform` module to get the new coordination and then via form factor formula to get the intensity. The total intensity after rotation is again via the element-wise multiplication of the rotated form factor array and initial structure factor. The spherical average method that includes all possible orientations of the model, is performed to obtain the 1D scattering profile by a numerically weighted histogram of the total intensity 3D array, i.e., given a small increment of Δq at q , $I_{1D}(q) = \text{Sum}(I_{3D}(\mathbf{q})) / \text{the number of voxel within } \Delta q \text{ at } q$.^[32] The source code of the calculation is freely available via the link <https://github.com/spectro-scatter/Nanocube-packing>.

Supporting Information

Supporting Information is available from the Wiley Online Library or from the author.

Acknowledgements

The authors acknowledge the Swedish Research Council (VR, grant numbers 2018–06378 and 2019–05624) for funding this work. This work was also supported by the Postdoctoral Researcher funding of Academy of Finland (330214), the New National Excellence Program Hungarian Ministry of Human Capacities (UNKP-21-5), and the Janos Bolyai Research Scholarship of the Hungarian Academy of Sciences. The authors thank Y. Zhong for assistance with TEM measurements, and M. Segad, and P. Munier, for assistance with the acquisition of SAXS data. The authors are also grateful to T. Plivelic from the CoSAXS beamline at MAX IV for providing the ultrasonic levitator and S. Disch from University of Cologne for providing the superball plugin mode in SasView. The authors acknowledge DESY (Hamburg, Germany), a member of the Helmholtz Association HGF, for the provision of experimental facilities. Parts of this research were carried out at PETRA III and The authors would like to thank W. Ohm for assistance using beamline P03. Beamtime was allocated for proposal I-20180345 EC. The research leading to this result has been supported by the project CALIPSOplus under the Grant Agreement 730872 from the EU Framework Programme for Research and Innovation HORIZON 2020. This work benefited from the use of the SasView application, originally developed under NSF award DMR-0520547. SasView also contains code developed with funding from the European Union's Horizon 2020 research and innovation program under the SINE2020 project, grant agreement No 654000. Z. P. Lv also offers sincere condolence to Dr. Long Cui, his former colleague and close friend, who passed away in a deplorable accident.

Conflict of Interest

The authors declare no conflict of interest.

Data Availability Statement

The data that support the findings of this study are available from the corresponding author upon reasonable request.

Keywords

anisotropic nanoparticles, small angle X-ray scattering, superlattice transformation, time-dependent measurements

Received: November 4, 2021

Revised: April 14, 2022

Published online: May 6, 2022

- [1] H. Cölfen, M. Antonietti, *Angew. Chem., Int. Ed.* **2005**, *44*, 5576.
- [2] K. Deng, Z. Luo, L. Tan, Z. Quan, *Chem. Soc. Rev.* **2020**, *49*, 6002.
- [3] G. Rainò, M. A. Becker, M. I. Bodnarchuk, R. F. Mahrt, M. V. Kovalenko, T. Stöferle, *Nature* **2018**, *563*, 671.
- [4] Y. Tong, E.-P. P. Yao, A. Manzi, E. Bladt, K. Wang, M. Döblinger, S. Bals, P. Müller-Buschbaum, A. S. Urban, L. Polavarapu, J. Feldmann, *Adv. Mater.* **2018**, *30*, 1801117.
- [5] L. Wu, P.-O. Jubert, D. Berman, W. Imano, A. Nelson, H. Zhu, S. Zhang, S. Sun, *Nano Lett.* **2014**, *14*, 3395.
- [6] S. Disch, E. Wetterskog, R. P. Hermann, D. Korolkov, P. Busch, P. Boesecke, O. Lyon, U. Vainio, G. Salazar-Alvarez, L. Bergström, T. Brückel, *Nanoscale* **2013**, *5*, 3969.
- [7] J. Henzie, M. Grünwald, A. Widmer-Cooper, P. L. Geissler, P. Yang, *Nat. Mater.* **2012**, *11*, 131.
- [8] M. N. O'Brien, M. R. Jones, C. A. Mirkin, *Proc. Natl. Acad. Sci.* **2016**, *113*, 11717.
- [9] J. J. Choi, C. R. Bealing, K. Bian, K. J. Hughes, W. Zhang, D. M. Smilgies, R. G. Hennig, J. R. Engstrom, T. Hanrath, *J. Am. Chem. Soc.* **2011**, *133*, 3131.
- [10] K. J. Si, Y. Chen, Q. Shi, W. Cheng, *Adv. Sci.* **2018**, *5*, 1700179.
- [11] K. Bian, J. J. Choi, A. Kaushik, P. Clancy, D.-M. Smilgies, T. Hanrath, *ACS Nano* **2011**, *5*, 2815.
- [12] M. R. Jones, K. D. Osberg, R. J. Macfarlane, M. R. Langille, C. A. Mirkin, *Chem. Rev.* **2011**, *111*, 3736.
- [13] P. F. Damasceno, M. Engel, S. C. Glotzer, *Science* **2012**, *337*, 453.
- [14] B. W. Goodfellow, B. A. Korgel, *ACS Nano* **2011**, *5*, 2419.
- [15] Y. Yu, D. Yu, C. A. Orme, *Nano Lett.* **2017**, *17*, 3862.
- [16] H. Chan, A. Demortière, L. Vukovic, P. Král, C. Petit, *ACS Nano* **2012**, *6*, 4203.
- [17] Z. Quan, W. Siu Loc, C. Lin, Z. Luo, K. Yang, Y. Wang, H. Wang, Z. Wang, J. Fang, *Nano Lett.* **2012**, *12*, 4409.
- [18] Y. Zhang, F. Lu, D. van der Lelie, O. Gang, *Phys. Rev. Lett.* **2011**, *107*, 135701.
- [19] J. J. Choi, K. Bian, W. J. Baumgardner, D.-M. Smilgies, T. Hanrath, *Nano Lett.* **2012**, *12*, 4791.
- [20] M. C. Dalfovo, L. J. Giovanetti, J. M. Ramallo-López, R. C. Salvarezza, F. G. Requejo, F. J. Ibañez, *J. Phys. Chem. C* **2015**, *119*, 5098.
- [21] B. W. Goodfellow, M. R. Rasch, C. M. Hessel, R. N. Patel, D. M. Smilgies, B. A. Korgel, *Nano Lett.* **2013**, *13*, 5710.
- [22] M. Agthe, T. S. Plivelic, A. Labrador, L. Bergström, G. Salazar-Alvarez, *Nano Lett.* **2016**, *16*, 6838.
- [23] M. Kapuscinski, M. Agthe, Z.-P. P. Lv, Y. Liu, M. Segad, L. Bergström, *ACS Nano* **2020**, *14*, 5337.
- [24] M. C. Weidman, D.-M. Smilgies, W. A. Tisdale, *Nat. Mater.* **2016**, *15*, 775.
- [25] Y. Nagaoka, R. Tan, R. Li, H. Zhu, D. Eggert, Y. A. Wu, Y. Liu, Z. Wang, O. Chen, *Nature* **2018**, *561*, 378.
- [26] R. Li, J. Zhang, R. Tan, F. Gerdes, Z. Luo, H. Xu, J. A. Hollingsworth, C. Klinke, O. Chen, Z. Wang, *Nano Lett.* **2016**, *16*, 2792.
- [27] I. Lokteva, M. Koof, M. Walther, G. Grübel, F. Lehmkuhler, *Small* **2019**, *15*, 1900438.
- [28] I. Lokteva, M. Dartsch, F. Dallari, F. Westermeier, M. Walther, G. Grübel, F. Lehmkuhler, *Chem. Mater.* **2021**, *33*, 6553.
- [29] Z.-P. Lv, M. Kapuscinski, L. Bergström, *Nat. Commun.* **2019**, *10*, 4228.
- [30] D. Dresen, A. Qdemat, S. Ulusoy, F. Mees, D. Zákutná, E. Wetterskog, E. Kentzinger, G. Salazar-Alvarez, S. Disch, *J. Phys. Chem. C* **2021**, *125*, 23356.
- [31] S. Förster, L. Apostol, W. Bras, *J. Appl. Crystallogr.* **2010**, *43*, 639.
- [32] K. G. Yager, Y. Zhang, F. Lu, O. Gang, *J. Appl. Crystallogr.* **2014**, *47*, 118.
- [33] R. Li, K. Bian, Y. Wang, H. Xu, J. A. Hollingsworth, T. Hanrath, J. Fang, Z. Wang, *Nano Lett.* **2015**, *15*, 6254.
- [34] F. Dekker, B. W. M. Kuipers, A. V. Petukhov, R. Tuinier, A. P. Philipse, *J. Colloid Interface Sci.* **2020**, *571*, 419.
- [35] S. Leekumjorn, S. Gullapalli, M. S. Wong, *J. Phys. Chem. B* **2012**, *116*, 13063.
- [36] Z.-P. Lv, Z.-Z. Luan, H.-Y. Wang, S. Liu, C.-H. Li, D. Wu, J.-L. Zuo, S. Sun, *ACS Nano* **2015**, *9*, 12205.
- [37] X. M. Lin, H. M. Jaeger, C. M. Sorensen, K. J. Klabunde, *J. Phys. Chem. B* **2001**, *105*, 3353.
- [38] E. Dubois, V. Cabuil, F. Boué, R. Perzynski, *J. Chem. Phys.* **1999**, *111*, 7147.
- [39] S. W. Winslow, J. W. Swan, W. A. Tisdale, *J. Am. Chem. Soc.* **2020**, *142*, 9675.
- [40] J. Park, K. An, Y. Hwang, J. E. G. Park, H. J. Noh, J. Y. Kim, J. H. Park, N. M. Hwang, T. Hyeon, *Nat. Mater.* **2004**, *3*, 891.
- [41] S. V. Roth, G. Herzog, V. Körstgens, A. Buffet, M. Schwartzkopf, J. Perlich, M. M. Abul Kashem, R. Döhrmann, R. Gehrke, A. Rothkirch, K. Stassig, W. Wurth, G. Benecke, C. Li, P. Fratzl, M. Rawolle, P. Müller-Buschbaum, *J. Phys. Condens. Matter.* **2011**, *23*, 254208.
- [42] A. Buffet, A. Rothkirch, R. Döhrmann, V. Körstgens, M. M. Abul Kashem, J. Perlich, G. Herzog, M. Schwartzkopf, R. Gehrke, P. Müller-Buschbaum, S. V. Roth, *J. Synchrotron Radiat.* **2012**, *19*, 647.
- [43] C. Krywka, H. Neubauer, M. Priebe, T. Salditt, J. Keckes, A. Buffet, S. V. Roth, R. Döhrmann, M. Mueller, *J. Appl. Cryst.* **2012**, *45*, 85.
- [44] G. Benecke, W. Wagermaier, C. Li, M. Schwartzkopf, G. Flucke, R. Hoerth, I. Zizak, M. Burghammer, E. Metwalli, P. Müller-Buschbaum, M. Trebbin, S. Förster, O. Paris, S. V. Roth, P. Fratzl, *J. Appl. Crystallogr.* **2014**, *47*, 1797.
- [45] G. Járvas, J. Kontos, J. Hancsók, A. Dallos, *Int. J. Heat Mass Transfer* **2015**, *84*, 1019.
- [46] M. R. Jones, R. J. MacFarlane, B. Lee, J. Zhang, K. L. Young, A. J. Senesi, C. A. Mirkin, *Nat. Mater.* **2010**, *9*, 913.